# A vibration-based method to estimate the low-wavenumber wall pressure field in a turbulent boundary layer

Hesam Abtahi, Mahmoud Karimi, Laurent Maxit

25·29 August 2024
inter.noise
NANTES FRANCE

# A vibration-based method to estimate the low-wavenumber wall pressure field in a turbulent boundary layer

Hesam Abtahi[1]
Centre for Audio, Acoustics and Vibration, University of Technology Sydney, Sydney, Australia

Mahmoud Karimi[2]
Centre for Audio, Acoustics and Vibration, University of Technology Sydney, Sydney, Australia

Laurent Maxit[3]
Univ Lyon, INSA–Lyon, Laboratoire Vibrations-Acoustique (LVA), 25 bis, av. Jean Capelle, F-69621, Villeurbanne Cedex, France

**ABSTRACT**

*When an elastic structure is excited by a low-speed turbulent flow, it generates flow-induced vibration which is primarily due to the low-wavenumber components of the wall pressure field (WPF) beneath the turbulent boundary layer (TBL). Therefore, to accurately predict the vibration response of the structure, an accurate estimation of the low-wavenumber WPF is needed. While existing TBL models for WPF well predict the convective region, they exhibit significant discrepancies in predicting the low-wavenumber levels. This numerical study aims to explore the feasibility of estimation of the low-wavenumber WPF by analysing vibration data obtained from a structure excited by a TBL. An inverse method is proposed based on the relationship between the TBL forcing function and structural vibrations in the wavenumber domain. The random TBL force is simulated with deterministic loading using the uncorrelated wall plane wave technique. A model of a simply supported plate under a TBL excitation is developed to demonstrate the proposed method. The plate's acceleration data is then used to estimate the WPF in the low-wavenumber range. It is shown how using multiple discrete frequencies in the analysis can reduce the required snapshots for accurate estimation of the WPF.*

## 1. INTRODUCTION

In practical applications, it is crucial to comprehend the impact of flow-induced vibrations on structures, as it can lead to structural fatigue, flutter, and aeroelastic instability. Additionally, vibrations stemming from TBL-induced pressure fluctuations contribute to noise emissions, thereby affecting acoustic comfort and environmental quality. Consequently, gaining insights into the response of structures to TBL excitation is essential for devising effective design strategies aimed at mitigating flow-induced vibrations and enhancing overall environmental quality. The prediction of WPF in turbulent flows within TBL is challenging due to their random nature.

[1]Seyedhesamaldin.Abtahi@student.uts.edu.au

[2]Mahmoud.Karimi@uts.edu.au

[3]Laurent.Maxit@insa-lyon.fr

Relying solely on numerical simulations can be both computationally expensive and complex. As a result, researchers employ a hybrid approach, combining numerical simulations with empirical data derived from flow measurements, to develop semi-empirical TBL models that approximate the WPF beneath a TBL. However, the accuracy levels of the developed models vary.

As a considerable amount of TBL energy is conveyed through pressure fluctuations at the convective wavenumber, the convective wavenumber ($k_c = \omega/U_c$) has been deemed the crucial parameter dictating TBL-induced vibrations. However, in low Mach number flows where structures are excited by heavy fluids, it has been noted that the convective wavenumbers are excessively high to synchronize with the bending waves of the underlying structure, resulting in minimal vibrations. In such cases, the structural wavelength aligns with the low-wavenumber region of the WPF. As a result, the primary influence on the vibration response of the structure arises from the sub-convective region [1, 2]. Hence, precise estimation of the WPF within this frequency range is critical for accurately predicting TBL-induced vibrations.

While many wavenumber-frequency models perform well in predicting the convective region, disparities arise in the sub-convective domain [3–5]. This discrepancy has its origins in the challenges of modeling and measuring low-wavenumber levels due to their lower amplitudes compared to convective wavenumber levels of the WPF. Consequently, there is a notable variation in the sub-convective region among semi-empirical models. In this work, we aim to estimate the low-wavenumber components of the WPF using a vibration-based approach. This approach utilizes the structural wavenumber filtering capabilities of a structure in order to reconstruct the pressure field [2, 6–9].

The authors' recent work [9] delved into estimating the low-wavenumber WPF through a vibration-based approach. Utilizing a virtual vibration experiment employing the uncorrelated wall plane wave (UWPW) technique, we analyzed computed acceleration data at a single frequency to determine the minimum number of realizations necessary for accurate WPF estimation in the low-wavenumber domain. In this study, we propose a frequency band method aimed at reducing the required number of realizations by leveraging computed acceleration data across multiple discrete frequencies. However, when utilizing the frequency band method, we make the assumption that the auto-spectral density (ASD) of the WPF is known in advance, and furthermore, that the low-wavenumber components of the WPF remain independent of frequency within a narrow frequency range.

## 2. ANALYTICAL FORMULATION

In this section, we have detailed the process of estimating the WPF in the low-wavenumber domain through the utilization of the frequency band method. In this method, the cross-spectrum matrix (CSM) calculated for different frequencies within the frequency band of $[\omega_{\min} - \omega_{\max}]$ is utilized to estimate the WPF in the low-wavenumber domain. Prior to implementing this method, it is assumed that the ASD of the WPF ($\bar{\Psi}_{pp}(\omega)$) has been experimentally measured using a microphone array. Therefore, estimating the normalized CSD of the WPF is sufficient for the WPF estimation.

In Figure 1, the schematic diagram of the system under consideration is presented. In the upcoming subsection, the frequency band approach is introduced for the estimation of the WPF in the low-wavenumber domain.

### 2.1. Frequency Band Approach

In this section, we have detailed the process of estimating the WPF in the low-wavenumber domain through the utilization of the frequency band approach. The space-frequency spectrum of the plate acceleration, $S_{\gamma\gamma}(x, x', \omega)$, excited by the WPF can be expressed as follows [10]

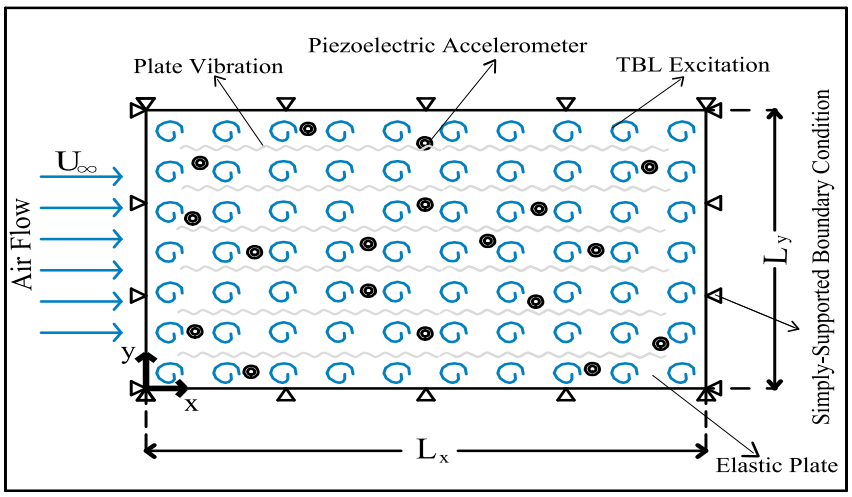


Figure 1: A Schematic diagram depicting the random array of accelerometers mounted on an elastic plate to record the plate's acceleration response to TBL-induced wall pressure fluctuations.

$$S_{\gamma\gamma}(\mathbf{x},\mathbf{x}',\omega) = \frac{1}{4\pi^2}\iint_{-\infty}^{\infty} H_\gamma(\mathbf{x},\mathbf{k},\omega)\phi_{pp}(\mathbf{k},\omega)H_\gamma^*(\mathbf{x}',\mathbf{k},\omega)\,dk, \tag{1}$$

where $H_\gamma(\mathbf{x},\mathbf{k},\omega)$ is the sensitivity function that characterizes the acceleration at point $\mathbf{x}$ when the plate is excited by a unit wall plane wave of wavevector $\mathbf{k}$ [9, 11]. Also, $\phi_{pp}(\mathbf{k},\omega)$ is the cross-spectrum density (CSD) function of TBL pressure in the wavenumber domain [10], and asterisk denotes the complex conjugate.

Using a rectangular rule to approximate the integration of Equation 1 by truncating and sampling the wavenumber space, one can compute the CSD of plate acceleration between two points $x_i$ and $x_j$ as follows

$$S_{\gamma\gamma}(\mathbf{x}_i,\mathbf{x}_j,\omega) = \frac{1}{4\pi^2}\sum_{l=1}^{N_\mathbf{k}} H_\gamma(\mathbf{x}_i,\mathbf{k}_l,\omega)\phi_{pp}(\mathbf{k}_l,\omega)H_\gamma^*(\mathbf{x}_j,\mathbf{k}_l,\omega)\,\delta k_x \delta k_y, \tag{2}$$

where $\delta k_x$ and $\delta k_y$ represent the resolutions of the wavenumber domain in the streamwise and spanwise directions, respectively. The total number of points in the wavenumber space is denoted by $N_\mathbf{k} = N_{k_x} \times N_{k_y}$, where $N_{k_x}$ and $N_{k_y}$ represent the number of points considered in sampling the wavenumber space along the $x$ and $y$ axes, respectively. The wavevector at a discrete point $l$ is denoted as $\mathbf{k}_l = (k_{x,l}, k_{y,l})$. Moreover, the CSD of the WPF as indicated in Equation 1 can be calculated according to Graham's method [4, 12] by employing various models for the ASD of the pressure field, $\bar{\Psi}_{pp}(\omega)$, and the normalized CSD of the pressure field, $\bar{\phi}_{pp}(\mathbf{k},\omega)$, separately. Normalizing the wavenumber values in the CSD of the WPF with respect to $k_c = \frac{\omega}{U_c}$, the Graham's formulation can be expressed to the following equation

$$\phi_{pp}(\bar{\mathbf{k}},\omega) = \bar{\Psi}_{pp}(\omega)\bar{\phi}_{pp}(\bar{\mathbf{k}}), \tag{3}$$

where $\bar{\mathbf{k}}$ is the normalized wavenumber (i.e. $\bar{\mathbf{k}} = \frac{\mathbf{k}}{k_c}$). Introducing Equation 3 in Equation 2 leads to the following equation for the CSD of the plate acceleration

$$S_{\gamma\gamma}(\mathbf{x}_i,\mathbf{x}_j,\omega) = \frac{1}{4\pi^2}\sum_{l=1}^{N_{\bar{\mathbf{k}}_l}} H_\gamma(\mathbf{x}_i,\frac{\omega\bar{\mathbf{k}}_l}{U_c},\omega)\bar{\Psi}_{pp}(\omega)\bar{\phi}_{pp}(\bar{\mathbf{k}}_l)H_\gamma^*(\mathbf{x}_j,\frac{\omega\bar{\mathbf{k}}_l}{U_c},\omega)\,\delta\bar{k}_x\delta\bar{k}_y. \tag{4}$$

We define the CSD for plate acceleration between every combination of sensors in an array of $N_s$ sensors as $S_{\gamma\gamma}(\mathbf{x}_i,\mathbf{x}_j,\omega)$, where $i,j \in \{1,N_s\}$. These computed CSDs are then stored in a

vector denoted as $\bar{S}_\gamma$, known as the acceleration CSD vector. The elements of $\bar{S}_\gamma$ are arranged such that the first $N_s$ components correspond to $S_{\gamma\gamma}(\mathbf{x}_1, \mathbf{x}_j, \omega)$ with $j \in \{1, N_s\}$, the subsequent $N_s$ components correspond to $S_{\gamma\gamma}(\mathbf{x}_2, \mathbf{x}_j, \omega)$ with $j \in \{1, N_s\}$, and so on:

$$\bar{S}_\gamma(\omega) = \begin{bmatrix} S_{\gamma\gamma}(\mathbf{x}_1, \mathbf{x}_1, \omega) \\ S_{\gamma\gamma}(\mathbf{x}_1, \mathbf{x}_2, \omega) \\ \vdots \\ S_{\gamma\gamma}(\mathbf{x}_i, \mathbf{x}_j, \omega) \\ \vdots \\ S_{\gamma\gamma}(\mathbf{x}_{N_s}, \mathbf{x}_{N_s-1}, \omega) \\ S_{\gamma\gamma}(\mathbf{x}_{N_s}, \mathbf{x}_{N_s}, \omega) \end{bmatrix}_{N_s^2 \times 1} . \tag{5}$$

Given that the CSD of the plate acceleration between various sensors can be approximated using Equation 2, we can express it in a more concise form as follows

$$\bar{S}_\gamma(\omega) = \bar{Q}(\omega)\bar{\Phi}_{pp}(\omega), \tag{6}$$

where $\bar{\Phi}_{pp}$ is a vector consisting of the unknown components of the normalized CSD of the WPF, presented as a function of the normalized wavenumbers as follows

$$\bar{\Phi}_{pp}(\omega) = \begin{bmatrix} \bar{\phi}_{pp}(\bar{k}_{x,1}, \bar{k}_{y,1}, \omega) \\ \bar{\phi}_{pp}(\bar{k}_{x,1}, \bar{k}_{y,2}, \omega) \\ \vdots \\ \bar{\phi}_{pp}(\bar{k}_{x,l}, \bar{k}_{y,l}, \omega) \\ \vdots \\ \bar{\phi}_{pp}(\bar{k}_{x,N_{k_x}}, \bar{k}_{y,N_{k_y}-1}, \omega) \\ \bar{\phi}_{pp}(\bar{k}_{x,N_{k_x}}, \bar{k}_{y,N_{k_y}}, \omega) \end{bmatrix}_{N_k \times 1} . \tag{7}$$

The elements of $\bar{\Phi}_{pp}$ are arranged in such a way that the initial $N_{k_y}$ components correspond to $\bar{\phi}_{pp}(\bar{k}_{x,1}, \bar{k}_{y,l}, \omega)$ with $l \in \{1, N_{k_y}\}$, the subsequent $N_{k_y}$ components correspond to $\bar{\phi}_{pp}(\bar{k}_{x,2}, \bar{k}_{y,l}, \omega)$ with $l \in \{1, N_{k_y}\}$, and so forth. Additionally, $\bar{Q}$ represents an excitation-response matrix with the following elements

$$\bar{Q} = \frac{\bar{\Psi}_{pp}(\omega)\delta\bar{k}_x\delta\bar{k}_y}{4\pi^2} \begin{bmatrix} H_\gamma(\mathbf{x}_1, \frac{\omega\bar{\mathbf{k}}_1}{U_c}, \omega)H_\gamma^*(\mathbf{x}_1, \frac{\omega\bar{\mathbf{k}}_1}{U_c}, \omega) & \cdots & H_\gamma(\mathbf{x}_1, \frac{\omega\bar{\mathbf{k}}_{N_{\bar{\mathbf{k}}}}}{U_c}, \omega)H_\gamma^*(\mathbf{x}_1, \frac{\omega\bar{\mathbf{k}}_{N_{\bar{\mathbf{k}}}}}{U_c}, \omega) \\ H_\gamma(\mathbf{x}_1, \frac{\omega\bar{\mathbf{k}}_1}{U_c}, \omega)H_\gamma^*(\mathbf{x}_2, \frac{\omega\bar{\mathbf{k}}_1}{U_c}, \omega) & & \vdots \\ \vdots & H_\gamma(\mathbf{x}_i, \frac{\omega\bar{\mathbf{k}}_l}{U_c}, \omega)H_\gamma^*(\mathbf{x}_j, \frac{\omega\bar{\mathbf{k}}_l}{U_c}, \omega) & \vdots \\ \vdots & & H_\gamma(\mathbf{x}_{N_s}, \frac{\omega\bar{\mathbf{k}}_{N_{\bar{\mathbf{k}}}}}{U_c}, \omega)H_\gamma^*(\mathbf{x}_{N_s-1}, \frac{\omega\bar{\mathbf{k}}_{N_{\bar{\mathbf{k}}}}}{U_c}, \omega) \\ H_\gamma(\mathbf{x}_{N_s}, \frac{\omega\bar{\mathbf{k}}_1}{U_c}, \omega)H_\gamma^*(\mathbf{x}_{N_s}, \frac{\omega\bar{\mathbf{k}}_1}{U_c}, \omega) & \cdots & H_\gamma(\mathbf{x}_{N_s}, \frac{\omega\bar{\mathbf{k}}_{N_{\bar{\mathbf{k}}}}}{U_c}, \omega)H_\gamma^*(\mathbf{x}_{N_s}, \frac{\omega\bar{\mathbf{k}}_{N_{\bar{\mathbf{k}}}}}{U_c}, \omega) \end{bmatrix}_{N_s^2 \times N_{\bar{\mathbf{k}}}} . \tag{8}$$

For a particular excitation frequency, the calculation of the vector $\bar{S}_\gamma$ relies on the plate's vibrational response to the TBL forcing function. According to the this procedure, we end up with $N_s^2$ equations for the $N_{k_x} \times N_{k_y}$ unknown coefficients outlined in Equation 6. Typically, the number of unknowns $N_{k_x} \times N_{k_y}$ surpasses the number of equations $N_s^2$. Consequently, Equation 6 represents an under-determined system and the system of equations has no unique solution. Also, matrix $\bar{Q}$ in Equation 8 is not a square matrix, and therefore, standard matrix inversion methods cannot be directly applied to it for computing the $\bar{\Phi}_{pp}$.

It's noteworthy that the low-wavenumber domain under investigation in this study is defined within the range of the plate's flexural wavenumber ($-k_b \leq k_x, k_y \leq k_b$). The flexural wavenumber $k_b$ of a plate is given by [13]

$$k_b = \sqrt[4]{\frac{12\rho_s(1-\nu^2)}{Eh^2}}\sqrt{\omega}. \tag{9}$$

The normalized domain corresponds to low-wavenumber domain is $\bar{k}_{x,LW}, \bar{k}_{y,LW} \in [\frac{-U_c k_b}{\omega}, \frac{U_c k_b}{\omega}]$. Since $k_b \propto \sqrt{\omega}$, normalized low-wavenumber domain is proportional to $\bar{k}_{x,LW}, \bar{k}_{y,LW} \propto \frac{1}{\sqrt{\omega}}$. This signifies that as the excitation frequency increases, the extent of the low-wavenumber domain diminishes. Therefore, to define a fixed low-wavenumber domain using this method, the low-wavenumber domain corresponding to $\omega_{\min}$ within the frequency band is chosen as the target domain for estimation. This selection encompasses the low-wavenumber domain linked to the higher frequency in the given frequency band.

The vector $\bar{S}_\gamma$ and matrix $\bar{Q}$ in Equation 6 are frequency-dependent. Given the assumption made by Martin and Leehey [6] and Bonness et al. [2] in their studies, one could posit that the frequency-independent nature of $\bar{\Phi}_{pp}$ holds true within the low-wavenumber domain across a small frequency band (i.e. $[\omega_{\min} - \omega_{\max}]$). Therefore, by taking into account $N_f$ discrete frequencies within the frequency band, $\bar{\Phi}(\omega_i) \approx \bar{\Phi}_{pp}^{[\omega_{\min},\omega_{\max}]}$, where $i \in \{1, N_f\}$. Utilizing the results of $\bar{S}_\gamma(\omega_i)$ and $\bar{Q}(\omega_i)$ at different frequencies, we can derive the following set of equations

$$\begin{bmatrix} \bar{S}_\gamma(\omega_1) \\ \bar{S}_\gamma(\omega_2) \\ \vdots \\ \bar{S}_\gamma(\omega_{N_f}) \end{bmatrix} = \bar{\Phi}_{pp}^{[\omega_{\min},\omega_{\max}]} \begin{bmatrix} \bar{Q}(\omega_1) \\ \bar{Q}(\omega_2) \\ \vdots \\ \bar{Q}(\omega_{N_f}) \end{bmatrix}. \tag{10}$$

If the number of frequencies is such that $N_s^2 \times N_f$ is larger than the size of $N_{k_x} \times N_{k_y}$, then the system will be overdetermined, and the matrix $\bar{Q}$ that needs to be inverted will be better conditioned. The objective is to seek an approximate solution for $\bar{\phi}_{pp}^{[\omega_{\min},\omega_{\max}]}$ within the low-wavenumber domain, aiming to minimize the residuals of the Equation 6. To achieve this, a regularization technique can be employed to estimate the WPF in the low-wavenumber domain, as suggested in [14].

### 2.2. Virtual Vibration Experiments

The Performance of the proposed approach can be assessed numerically by comparing the estimated WPF with a known reference input WPF. This evaluation involves exciting the plate with a predetermined forcing function and applying Equation 10 to the resulting vibration response. In this study, a virtual model is utilized to simulate the TBL excitation. To achieve this, the TBL excitation force is simulated through deterministic loading, employing the UWPW technique as described in [15]. This technique aims to replicate experimental scenarios by synthesizing TBL wall pressure. Subsequently, the deterministic forcing function is utilized to compute the plate's acceleration response, utilizing the ensemble average of various realizations of wall pressure. The pressure beneath the TBL for the $r$th realization is characterized by a series of UWPWs at a specific point $(x_M, y_M)$ on the plate, as detailed in [11, 15, 16].

$$p^r(x_M, y_M, \omega) = \sum_{l=1}^{N_k} \sqrt{\frac{\bar{\phi}_{pp}(\bar{k}_{x,l}, \bar{k}_{y,l}, \omega)\delta\bar{k}_x\delta\bar{k}_y}{4\pi^2}} e^{\mathrm{j}(\bar{k}_{x,l}x_M + \bar{k}_{y,l}y_M + \theta_l^r)}, \tag{11}$$

where $\theta$ represents a random phase uniformly distributed within the range $[0, 2\pi]$. Utilizing the modal expansion technique, the acceleration response of a plate at the specified point $(x_M, y_M)$

for a given frequency $\omega$, caused by the wall pressure (Equation 11), corresponding to the $r$th realization at each sensor location, can be derived by [15].

$$\gamma^r(x_M, y_M, \omega) = -\omega^2 \sum_{m=1}^{M} \sum_{n=1}^{N} \frac{F^r_{mn}(\omega)\varphi_{mn}(x_M, y_M)}{\Omega(\omega^2_{mn} - \omega^2 + \mathrm{j}\eta\omega\omega_{mn})}, \tag{12}$$

where the modal forces are given by

$$F^r_{mn} = \sum_{l=1}^{N_{\mathbf{k}}} \sqrt{\frac{\bar{\phi}_{pp}(\bar{k}_{x,l}, \bar{k}_{y,l}, \omega)\delta\bar{k}_x\delta\bar{k}_y}{4\pi^2}}\, e^{\mathrm{j}\theta^r_l} \psi_{mn}(\bar{k}_{x,l}, \bar{k}_{y,l}). \tag{13}$$

The CSD of acceleration between two points of $\mathbf{x}_i$ and $\mathbf{x}_j$ using the UWPW technique can be computed as follows

$$S_{\gamma\gamma}(\mathbf{x}_i, \mathbf{x}_j, \omega) = \frac{1}{N_r} \sum_{r=1}^{N_r} \gamma^r(x_i, y_i, \omega)\gamma^{*r}(x_j, y_j, \omega), \tag{14}$$

where $N_r$ is number of realizations. In the following section, we assess the results obtained from employing the proposed method to estimate the WPF in the low-wavenumber domain.

## 3. RESULTS AND DISCUSSION

This section utilizes the analytical formulations described in Section 2 to assess the WPF within the low-wavenumber range. To demonstrate the effectiveness of the suggested approach, we analyze the performance using the identical plate characteristics and TBL properties as studied in [9].

This study employs the Goody model to evaluate the ASD function of the WPF, and the Mellen model for the normalized CSD function. Equation 11 serves for simulating the input TBL forcing function. To simulate the TBL, Equation 2 needs a truncated number of wavenumbers in both the $x$ and $y$ directions. For this study, a cut-off wavenumber of $1.2k_c$ was chosen in both directions to accommodate the convective contributions of the TBL's WPF. Additionally, the wavenumber resolutions used for the WPF calculations should strike a balance: not too small to avoid increasing computational costs, yet not too large to skip main WPF values. In this study, the wavenumber resolution is fixed at $\delta k_x = \delta k_y = 5.6\ \mathrm{m}^{-1}$ for all examined frequencies.

In order to guarantee that the calculated CSD of the plate acceleration, measured by the virtual accelerometers, encompasses all significant modes, we opted to use $M = N = 50$ when computing $\bar{S}_\gamma(\omega)$ in Equation 2 through Equation 14. However, when calculating the $\bar{Q}$ matrix as expressed in Equation 8, we limit our consideration to the modes $M$ and $N$ within the frequency range $[0, 1.3\omega_{\max}]$. This choice is made as in practice, only resonant modes within a given frequency band can be reasonably estimated.

Figure 2 depicts the normalized CSD of a TBL WPF based on the Mellen model in the normalized wavenumber domain for the reference TBL at $f = 1400$ Hz. It's crucial to emphasize that the rectangular area shown in this figure indicates the low-wavenumber domain under investigation in this study.

To compute the TBL WPF, Equation 10 must be resolved. However, this equation falls under the category of ill-posed problems, meaning that even small perturbations in the input data can greatly impact the solution. Herein, the Truncated Generalized Singular Value Decomposition (TGSVD) technique is employed to estimate the WPF within the low-wavenumber domain. This is achieved by minimizing the 2-norm of the first derivative of the solution, as described in [14]. The regularization parameter, crucial for truncating the generalized singular value problem, is determined using the corner method. This technique utilizes an adaptive pruning algorithm to pinpoint the corner of a discrete L-curve produced by the TGSVD method [17].

This study assumes an irregular array of accelerometer to estimate the low-wavenumber WPF. The sensors arrangement remains consistent with that outlined in [9].

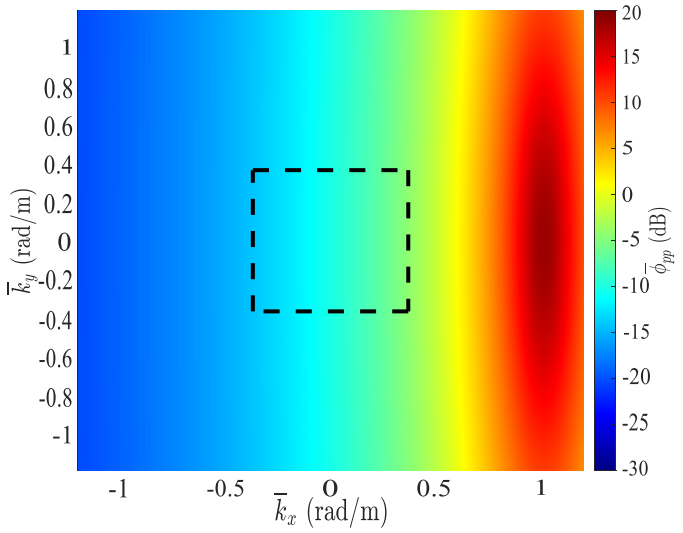


Figure 2: Contour plots of the Mellen wavenumber-frequency model for a flow speed of 50 m/s at 1400 Hz.

In this study, we consider the frequency band of $f = [1400 - 1475]$ Hz to estimate the WPF in the low-wavenumber domain, and subsequently compare the findings with those obtained using a single frequency of $f = 1400$ Hz in [9]. This method involves leveraging the CSM computed for various frequencies and employing these data to estimate the WPF. To transform the underdetermined system of equations in Equation 10 into an overdetermined system, a minimum of $N_f = 76$ frequency steps is required. Consequently, a frequency step of $df = 1$ Hz is adopted in this example to over-determine the system of equations.

To evaluate the effectiveness of the proposed method in estimating the TBL WPF, we calculate the mean absolute error (MAE) of the estimated WPF in the low-wavenumber domain relative to the reference input TBL model, which is based on the Mellen model (Figure 2). The MAE of the estimated WPF in the low-wavenumber domain is computed using the following formula

$$\text{MAE} = \frac{1}{N_{k_{LW}}} \sum_{l=1}^{N_{k_{LW}}} \left[ 10\mathbf{log}_{10}\left(\bar{\phi}_{pp}^{[\omega_{\min},\omega_{\max}]}(\bar{\mathbf{k}_l})\right)_e - 10\mathbf{log}_{10}\left(\bar{\phi}_{pp}^{[\omega_{\min},\omega_{\max}]}(\bar{\mathbf{k}_l})\right)_r \right], \quad \text{(dB)} \tag{15}$$

where $\left(\bar{\phi}_{pp}^{[\omega_{\min},\omega_{\max}]}(\bar{\mathbf{k}_l})\right)_e$ and $\left(\bar{\phi}_{pp}^{[\omega_{\min},\omega_{\max}]}(\bar{\mathbf{k}_l})\right)_r$ are the estimated and reference wavenumber-frequency spectrum of the WPF in the frequency band, respectively, and $N_{k_{LW}}$ corresponds to the total number of grid points in the low-wavenumber domain. Figures 3 (a), (c), and (e) illustrate the color maps of estimated normalized WPF using Equation 10 across the frequency range of $[1400 - 1475]$ Hz for varying numbers of realizations. Figure 3 (b), (d), and (f) illustrate the cross-sectional views of both the reference and estimated WPF at $\bar{k}_y = 0$. Two red-dashed lines in the figure represent the boundaries of the low-wavenumber domain. Moreover, the MAE values in decibels (dB) are presented for each case. The results shown in Figure 3 reveals that utilizing a group of closely spaced frequencies instead of a single frequency [9] reduces the required number of realizations to obtain a certain level of accuracy of the estimated WPF. For instance, when using the frequency band method, the MAE for $N_r = 5$ decreases from $\approx 5$ dB (obtained for the single frequency method in [9]) to 1.66 dB, indicating a good improvement. Moreover, doubling the number of realizations to $N_r = 10$ further reduces the MAE to 1.12 dB, indicating a reasonable level of accuracy in estimating the WPF. Figure 4 compares the MAE as a function of the number of sensors for different number of realizations, depicted separately for (a) a single frequency of $f = 1400$ Hz [9] and (b) a frequency band of $f = [1400 - 1475]$ HZ. These MAE values are compared with those obtained using the reference input TBL excitation (Ref. TBL). The findings

demonstrate that for accurate estimation of the low-wavenumber WPF at a single frequency of $f = 1400$ Hz with an MAE below 2 dB, over 300 realizations are necessary. In contrast, employing the frequency band method requires only 20 realizations to effectively estimate the WPF in the low-wavenumber domain. Moreover, it is evident that increasing the number of sensors does not yield substantial enhancements in the estimated WPF when a sufficient number of realizations are utilized in both scenarios. However, it is worth mentioning that in employing frequency band method, we have made two assumptions: (1) the ASD of the WPF is available beforehand through experimental measurements or computational fluid dynamics simulation, and (2) the WPF in the low-wavenumber domain is frequency independent within the small frequency range under consideration for implementing the proposed methodology.

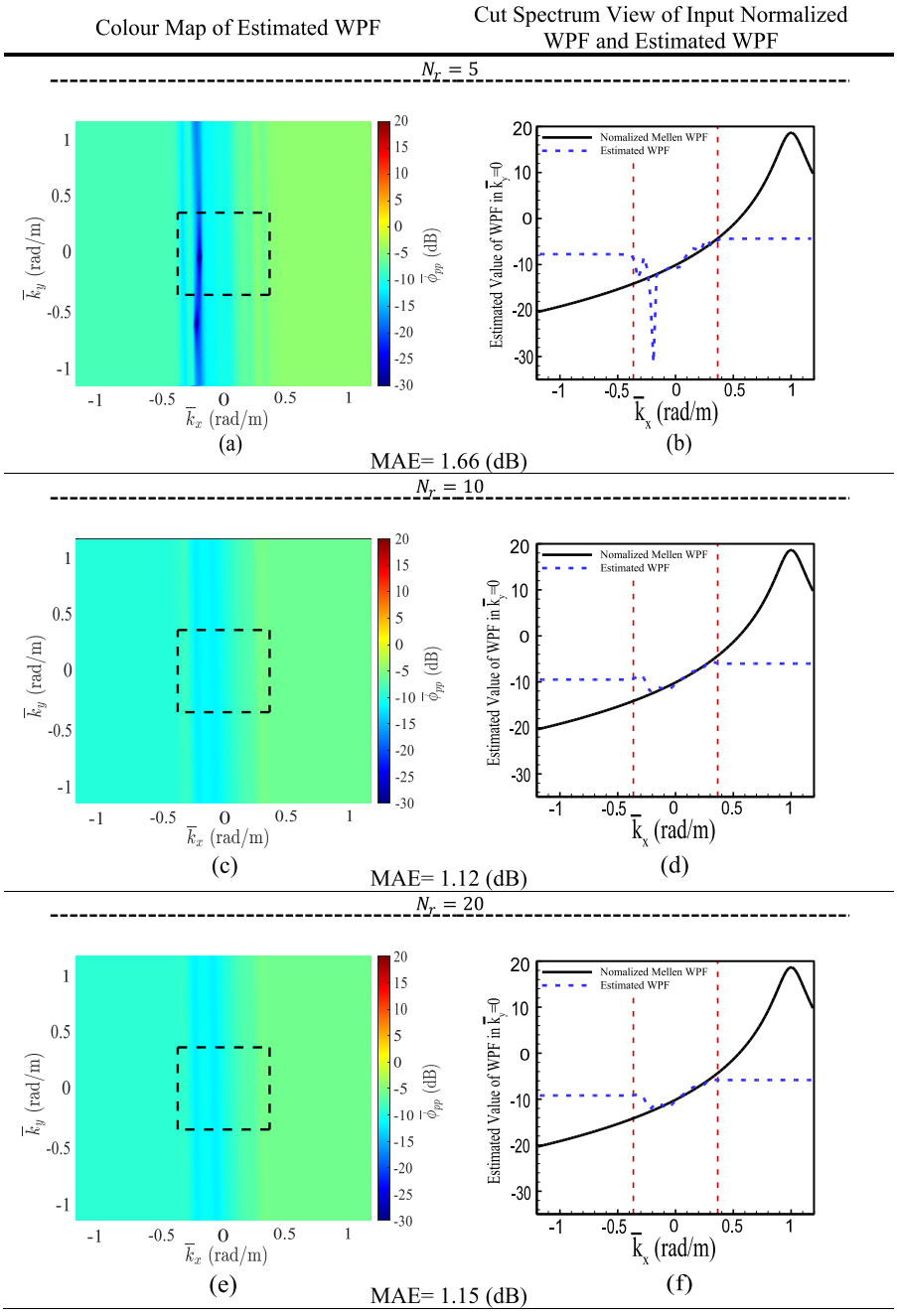


Figure 3: The estimated normalized WPF in frequency band of [1400 – 1475] Hz for an irregular array pattern with 10 sensors, shown for different numbers of realizations. The left-hand plots depict the color maps, while the right-hand plots display the 2D wavenumber-frequency spectra for $k_y = 0$. The MAE for each case is displayed in decibels (dB).

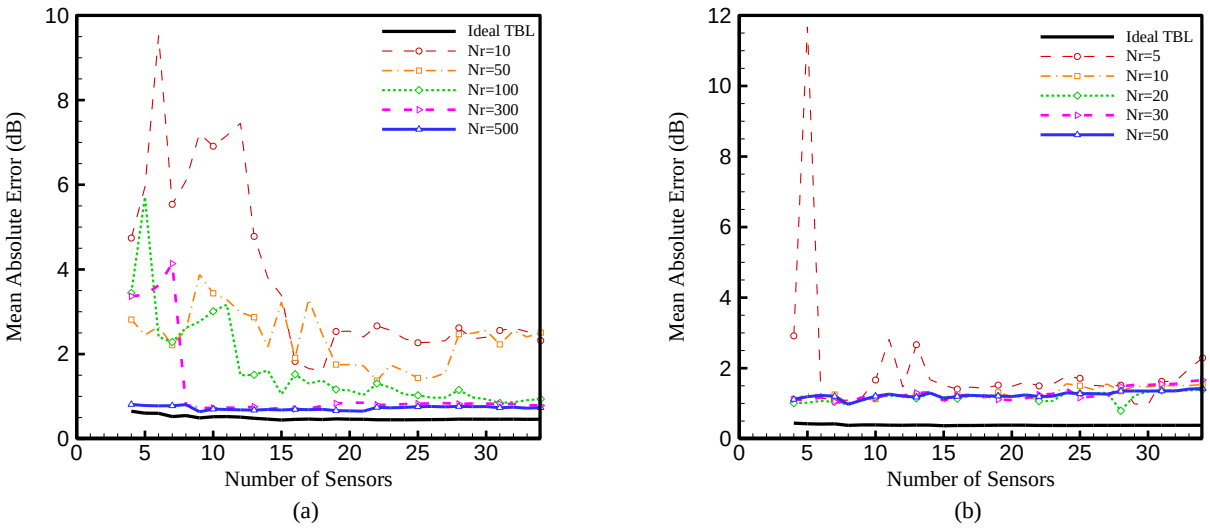


Figure 4: The comparison of MAE for the estimated WPF in the low-wavenumber domain as a function of number of sensors. The results highlight the impact of the number realization on accuracy of the estimated WPF for (a) single frequency of $f = 1400$ Hz [9] and (b) frequency band of $f = [1400 - 1475]$ Hz.

## 4. CONCLUSIONS

This study investigated the effectiveness of using a vibration-based method at multiple discrete frequencies for estimating the WPF in the low-wavenumber domain. The frequency band formulation with the assumption that the low-wavenumber WPF does not vary within the frequency band of interest was applied to identify the low-wavenumber levels of the WPF. It was found that few number of realizations is enough to accurately estimate the WPF in the low-wavenumber region using the frequency band method. This is advantageous in practice as only a few data samples need to be recorded at each frequency. Furthermore, it was observed that due to the filtering properties of the plate, the proposed method is limited to estimating the WPF within the low-wavenumber domain, and WPF outside of this domain cannot be estimated accurately.

## ACKNOWLEDGEMENTS

The first author acknowledges that this research is supported by the UTS President's Scholarship.

## REFERENCES

1. S. Hambric, Y. Hwang, and W. Bonness. Vibrations of plates with clamped and free edges excited by low-speed turbulent boundary layer flow.
2. W. Bonness, D. Capone, and S. Hambric. Low-wavenumber turbulent boundary layer wall-pressure measurements from vibration data on a cylinder in pipe flow. *Journal of Sound and Vibration*, 329(20):4166–4180, 2010.
3. W. Keith, D. Hurdis, and B. Abraham. A comparison of turbulent boundary layer wall-pressure spectra. *Journal of Fluids Engineering*, 114:338–347, 1992.
4. W. Graham. A comparison of models for the wavenumber–frequency spectrum of turbulent boundary layer pressures. *Journal of sound and vibration*, 206(4):541–565, 1997.
5. T. Miller, J. Gallman, and M. Moeller. Review of turbulent boundary layer models for acoustic analysis. *Journal of aircraft*, 49(6):1739–1754, 2012.

6. N. Martin and P. Leehey. Low wavenumber wall pressure measurements using a rectangular membrane as a spatial filter. *Journal of Sound and Vibration*, 52(1):95–120, 1977.
7. D. Lecoq, Ch. Pezerat, J. Thomas, and W. Bi. Extraction of the acoustic component of a turbulent flow exciting a plate by inverting the vibration problem. *Journal of Sound and Vibration*, 333(12):2505–2519, 2014.
8. Q. Leclere, A. Dinsenmeyer, E. Salze, and J. Antoni. A comparison between different wall pressure measurement devices for the separation and analysis of tbl and acoustic contributions. In *International Conference on Flow Induced Noise and Vibration Issues and Aspects*, pages 181–206. Springer, 2019.
9. H. Abtahi, M. Karimi, and L. Maxit. Identification of low-wavenumber wall pressure field beneath a turbulent boundary layer using vibration data. Available at SSRN: https://ssrn.com/abstract=4719145 or http://dx.doi.org/10.2139/ssrn.4719145.
10. C. Maury, P. Gardonio, and S. Elliott. A wavenumber approach to modelling the response of a randomly excited panel, part i: general theory. *Journal of Sound and Vibration*, 252(1):83–113, 2002.
11. M. Karimi, P. Croaker, L. Maxit, O. Robin, A. Skvortsov, S. Marburg, and N. Kessissoglou. A hybrid numerical approach to predict the vibrational responses of panels excited by a turbulent boundary layer. *Journal of Fluids and Structures*, 92:102814, 2020.
12. W. Graham. Boundary layer induced noise in aircraft, Part I: The flat plate model. *Journal of Sound and Vibration*, 192(1):101–120, 1996.
13. J. Guyader. *Vibration in continuous media*. John Wiley & Sons, 2013.
14. P. Hansen. Regularization tools version 4.0 for Matlab 7.3. *Numerical algorithms*, 46(2):189–194, 2007.
15. L. Maxit. Simulation of the pressure field beneath a turbulent boundary layer using realizations of uncorrelated wall plane waves. *The Journal of the Acoustical Society of America*, 140(2):1268–1285, 2016.
16. M. Karimi, P. Croaker, A. Skvortsov, D. Moreau, and N. Kessissoglou. Numerical prediction of turbulent boundary layer noise from a sharp-edged flat plate. *International Journal for Numerical Methods in Fluids*, 90(10):522–543, 2019.
17. P. Hansen, T. Jensen, and G. Rodriguez. An adaptive pruning algorithm for the discrete L-curve criterion. *Journal of computational and applied mathematics*, 198(2):483–492, 2007.